Supporting Information:

Spin Polarized Electron Dynamics Enhance Water Splitting Efficiency by Yttrium Iron Garnet Photoanodes: A New Platform for Spin Selective Photocatalysis

Harshad Gajapathy,[†] Savini Bandaranayake,[†] Emily Hruska,[†] Aravind Vadakkayil,[‡] Brian P. Bloom,[‡] Stephen Londo,[†] Jackson McClellan,[†] Jason Guo,[¶] Daniel Russell,[¶] Frank M. F. de Groot,[§] Fengyuan Yang,[¶] David H. Waldeck,[‡] Martin Schultze,[∥] and L. Robert Baker*,[†]

[†]Department of Chemistry and Biochemistry, The Ohio State University, Columbus, Ohio 43210, United States

[‡]Department of Chemistry, University of Pittsburgh, 15260 Pittsburgh, Pennsylvania, United States

[¶]Department of Physics, The Ohio State University, Columbus, Ohio 43210, United States

[§]Inorganic Chemistry and Catalysis, Debye Institute for Nanomaterials Science, Utrecht University, 3584CG Utrecht, The Netherlands

[∥]Institute of Experimental Physics, Graz University of Technology, Petersgasse 16, Graz 8010, Austria

E-mail: baker.2364@osu.edu

Contents

1. Sample characterization

YIG Preparation

YIG(20nm)/GGG thin films were grown using RF-sputtering. The substrate temperature was kept at 650 ℃. Chamber base pressure was ∼5e-8 torr and growths were done at an operating pressure of 11.5 mtorr in an Ar + 1% O_2 environment. The plasma was maintained using an 80W RF power supply.

Atomic Force Microscopy

A Bruker AXS Dimension Icon Atomic Force Microscope (AFM) with ScanAsyst, equipped with a TESPA-V2 cantilever, was used to measure the surface roughness of YIG(20nm)/GGG(111) film over a 2 x 2 μm^2 area, shown in Figure S1 (A). The root-mean-square roughness was determined to be 0.17 nm.

Magnetic Hysteresis Analysis

OOP magnetic hysteresis measurements were carried out using a Quantum Design MPMS3

SQUID Magnetometer in vibrating sample mode at room temperature, shown in Figure S1 (B). The magnetic hysteresis shows an OOP hard axis, which is consistent for YIG films on GGG(111).

X-Ray Reflectivity and X-Ray Diffraction

X-ray reflectivity and diffraction measurements were taken with Rigaku Smart-Lab with parallel beam mirror + Ge(220) 2-bounce monochromator. For reflectivity measurements, the sample was aligned at $2\theta = 1°$, and the presence of Kiessig fringes confirms a sample thickness of 20nm, shown in Figure S1 (C). For XRD measurements, the sample was aligned to the GGG(444) substrate peak, and the high-resolution scan shows the presence of Laue oscillations, indicating good sample crystallinity, shown in Figure S1 (D).
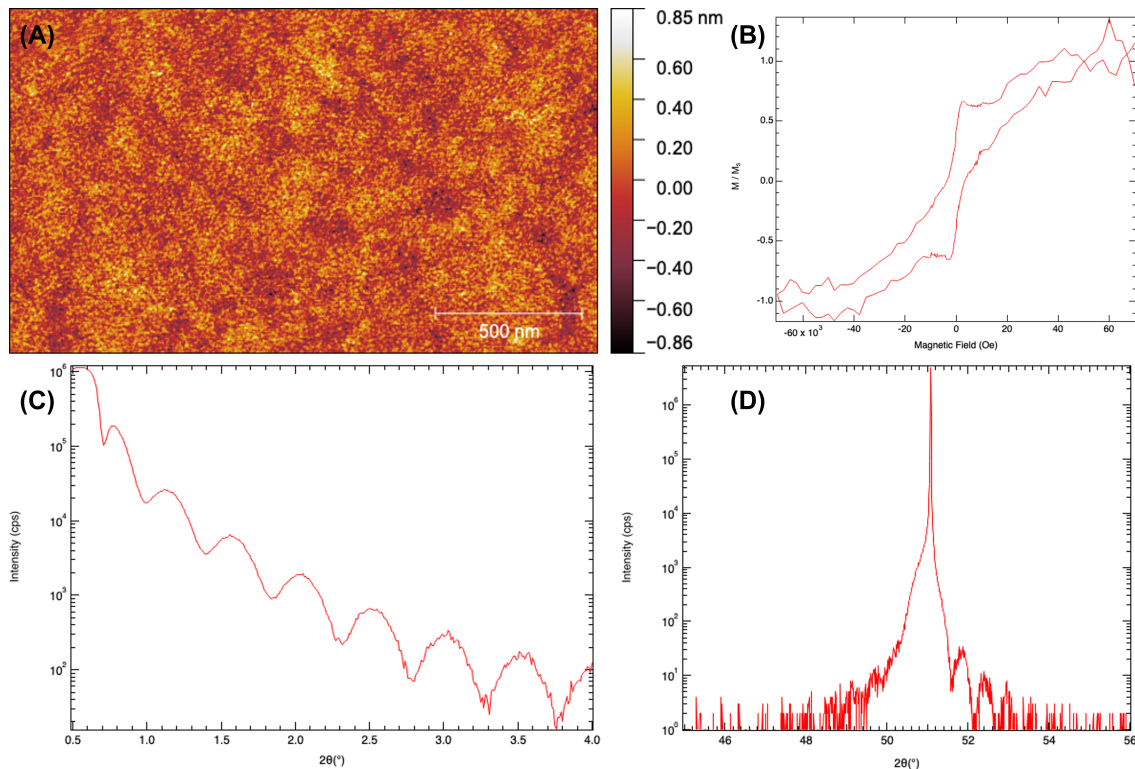
Figure S1: Characterization of Yttrium Iron Garnet using (A) atomic force microscopy, (B) magnetic hysteresis, (C) X-ray reflectivity, and (D) X-ray diffraction.

Raman and X-Ray Diffraction of Nanoparticles
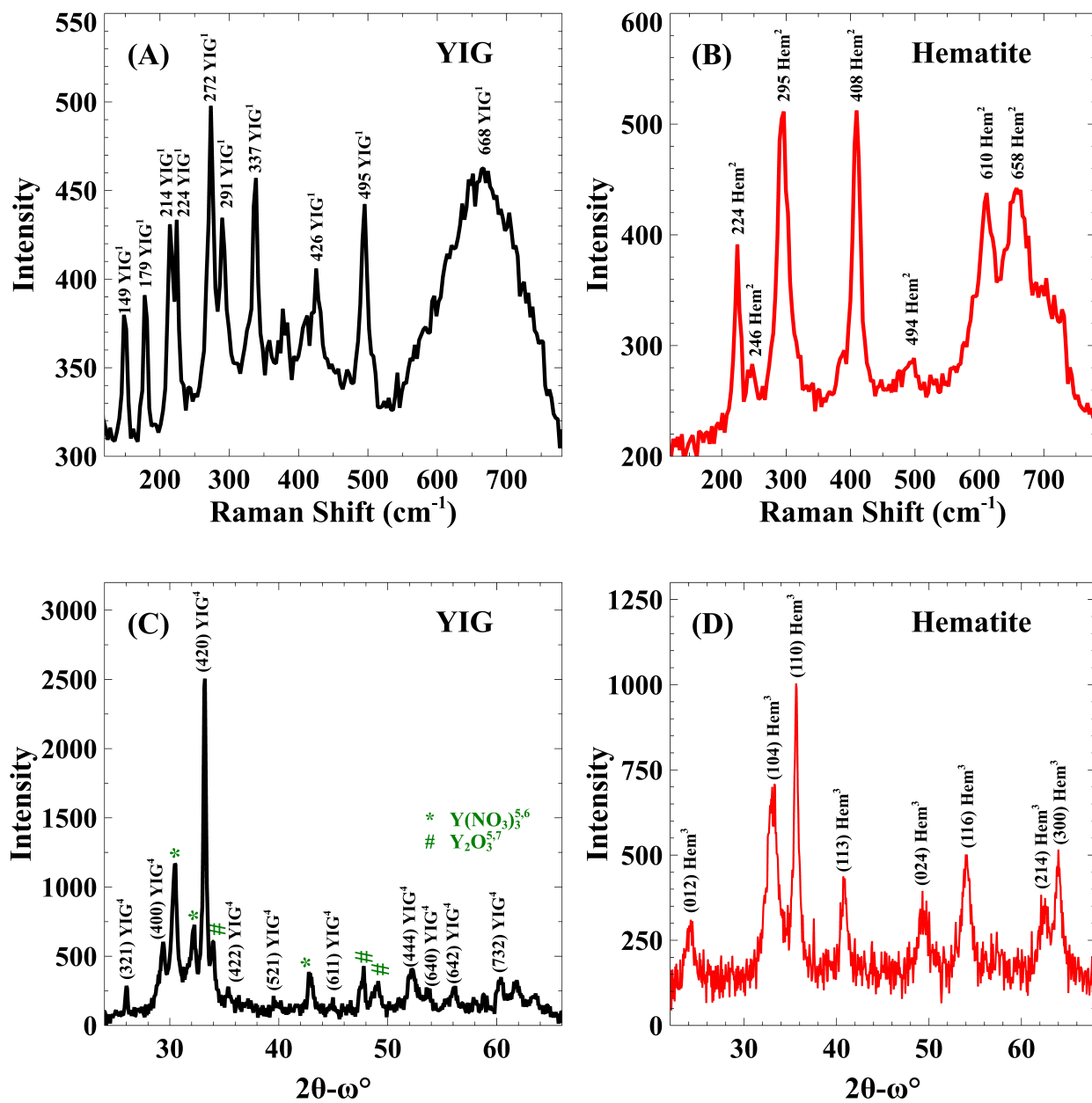
Figure S2: Characterizations of Yttrium Iron Garnet and hematite nanoparticles using (A, B) Raman spectroscopy and (C, D) X-ray diffraction.

Raman spectroscopy was performed on YIG and hematite nanoparticle samples using a Renishaw Raman instrument with a 532 nm excitation source. The results are shown in Figure S2 (A, B) where the peak positions for YIG[1] and hematite[2] exactly match their respective references. This shows the presence of YIG and hematite in the catalyst. The XRD of hematite and YIG are performed with Cu K-α frequency and shown in Figure S2 (C,

D). The XRD peaks for hematite match well with the reference.[3] For YIG, the XRD peaks of the nanoparticles match with the YIG nanoparticles prepared using the sol-gel method shown in Sharma et. al.,[4] where the primary peaks match YIG, and several additional peaks correspond to $Y(NO_3)_3$[5,6] and Y_2O_3[5,7] impurities. These impurities are from the synthesis of the nanoparticle, and they do not contribute to photoelectrochemical water splitting due to their UV band gap of 3.10 eV[6] and 4.10 eV[7] respectively. Additionally, $Y(NO_3)_3$ is water soluble and as such cannot contribute to the water splitting activity. From this, we conclude that hematite and YIG are the active phases of the respective water splitting catalysts.

Scanning Electron Microscopy of Nanoparticles
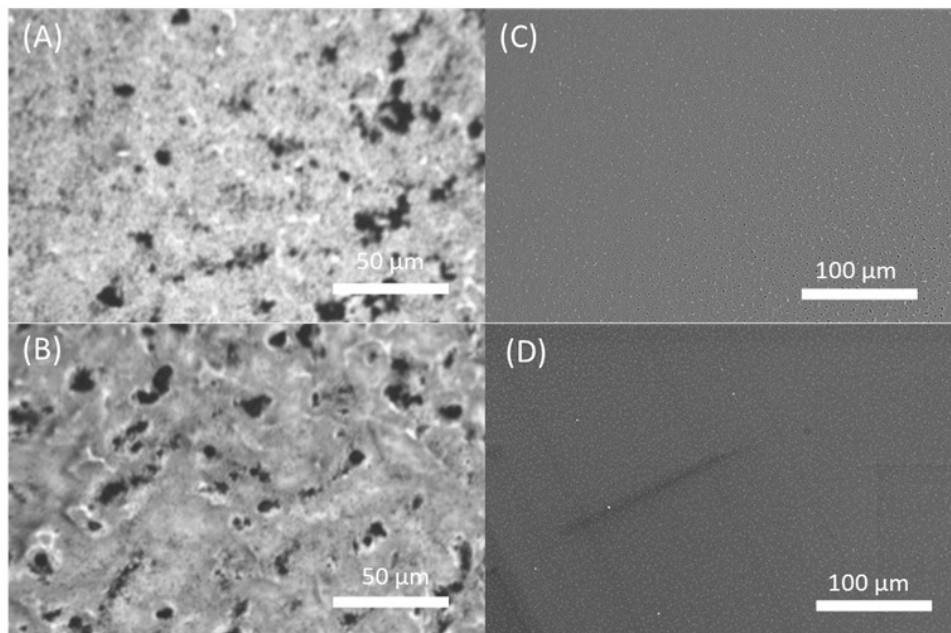
Figure S3: The optical microscope images of YIG (A) and hematite (B). Scanning electron microscope images of YIG (C) and hematite (D).

The surface morphology of YIG and hematite were characterized using optical and scanning electron microscopies as shown in Figure S3. These show that YIG and hematite have similar morphologies therefore the current enhancement is not due to morphological differences.

2. Photoelectrochemical measurements

Linear sweep voltammograms of the ring electrode without any catalyst deposition were taken in a potential range of -0.14 to 0.86 V vs RHE, by pumping oxygen into the 0.02 M phosphate buffer electrolyte. The close overlay of the two LSVs, one in the dark and the other with irradiation ensured that the photoexcitation of the ring electrode did not affect the results.
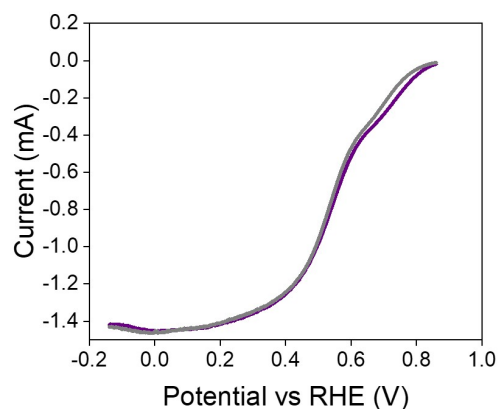
Figure S4: Linear sweep voltammograms for the ring electrode in the dark (purple) and with irradiation (grey)

A. Electrochemically accessible surface area
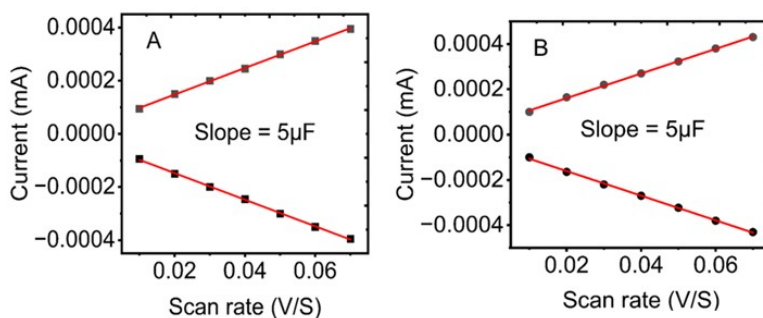
Figure S5: Representative double layer capacitance measurements for YIG (A) and Hematite (B) catalysts.

ECSA (Electrochemically accessible surface area) is given as C_{DL}/C_S, where C_{DL} is the double layer capacitance calculated from the slope of the current (mA) vs scan rate

(V/S) plot, and C_S is the specific capacitance of the sample (which is a constant). We have measured the C_S values for both hematite and YIG which are the same within error confirming that morphological differences in these two samples cannot explain the 15-fold photoactivity enhancement in YIG activity compared to hematite.

Average double layer capacitance (C_{DL}) of YIG $= 5.0 \pm 0.1$ μF

Average double layer capacitance (C_{DL}) of Hematite $= 5.2 \pm 0.3$ μF

B. Glassy Carbon Electrode
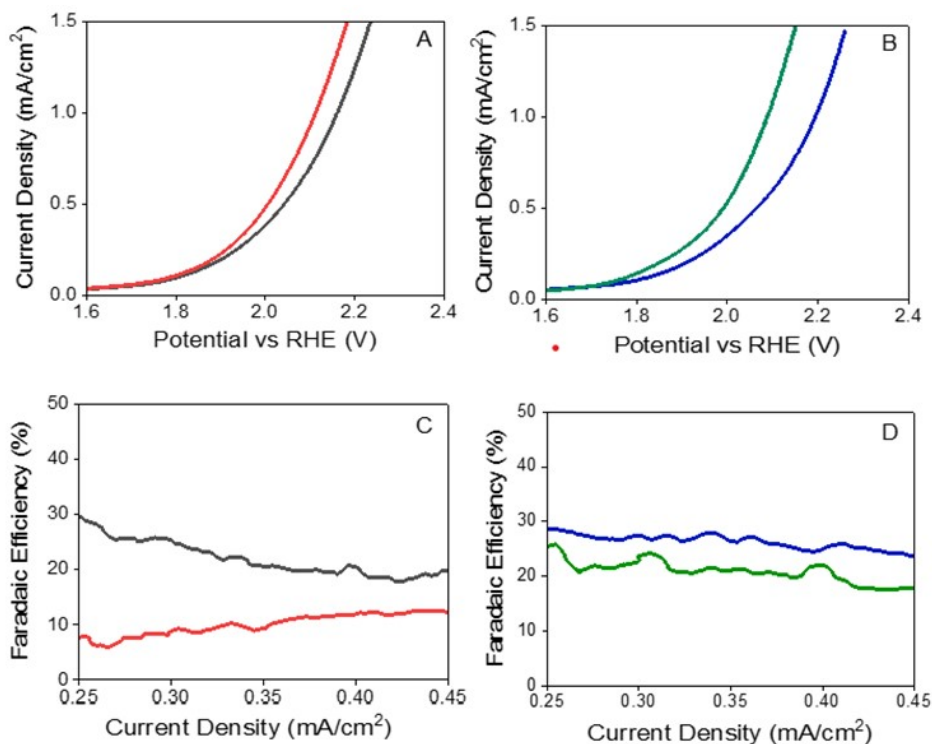
Figure S6: Linear sweep voltammograms for hematite (A) and YIG (B) catalyst-loaded glassy carbon electrodes in the dark (black, blue) and upon irradiation (red, green) respectively. Panels (C) and (D) plot the average Faradaic efficiency against the current density for hematite and YIG in dark (black, blue) and light (red, green) respectively.

We show the electrochemical measurements performed on glassy carbon electrodes above. Here, the same phenomenon is observed i.e., the YIG shows higher photocurrent and higher faradaic efficiency than hematite upon irradiation.

3. XUV-MCD ligand field multiplet simulations

A. MCD simulation

To simulate the XUV-MCD spectra for Fe^{3+} and Fe^{4+} atoms under T_d and O_h coordinations, CTM4XAS 5.5[8–11] program was used. The program was used to calculate the ground state MCD spectrum using the crystal field splitting, exchange field, and slater integral reduction parameters listed in Table 1. From the program, we obtained the sticks files with atomic multiplet structures for right and left circular polarized light. The stick spectrum for both right and left circular polarized light was broadened according to the Lorentz-Fano[12–14] line shape using the parameters listed in the table below. The Lorentzian line width (L) is equal to the minimum Lorentzian width (minL) below the Lorentzian cutoff (cutOff) and after the cutoff energy, it increases linearly by a factor of Lorentzian Broadening parameter (dL) times difference between energy (E) and cutoff as given by the formula:

$$L = minL + (E - cutOff) * dL$$

The Fano line shape is given by:

$$Fano = \frac{(q * (L/2) + \Delta E)^2}{(L/2)^2 + (\Delta E)^2}$$

where q is the Fano parameter, L is the Lorentzian line width and ΔE is the energy shift. The spectrum was converted to an absolute absorption cross-section by multiplying with a conversion parameter shown in the table based on values reported before,[13] which was scaled with the stoichiometry of each lattice.

   The imaginary part of the refractive index (k) was calculated from the absorption spectrum of right and left circular polarized light using the formula:

$$\kappa = \frac{\lambda \eta \sigma}{4\pi}$$

in which λ is the wavelength of light, η is the number density of absorbers (known from the bulk density of YIG), and σ is the absorption cross-section of the material. For the ground state simulation, the k values for Fe^{3+} T_d and O_h coordinations were added together to calculate a spectrum for both right and left circularly polarized light. For the excited state spectrum during illumination, contributions from Fe^{4+} T_d and O_h were also considered as described below. The real part of the refractive index (n) was calculated from k using the Kramers-Kronig relationship:

$$n\left(\omega\right) = 1 + \frac{2P}{\pi} \int_0^\infty \frac{\omega' k\left(\omega'\right)}{\omega'^2 - \omega^2} d\omega'$$

where ω represents angular frequency of light, ω' represents range of the calculation, and P is the Cauchy principle value. An offset of -0.5 was added to n to account for the universal negative permittivity to materials in the XUV spectral range.[15] Values of n and k were combined to obtain the complex refractive index (N) for both circular polarizations of light. This N was used to calculate reflectance (r) using the Fresnel equation:

$$r_p = \frac{N^2 \cos\theta - \sqrt{N^2 - \sin^2\theta}}{N^2 \cos\theta + \sqrt{N^2 - \sin^2\theta}}$$

$$r_s = \frac{\cos\theta - \sqrt{N^2 - \sin^2\theta}}{\cos\theta + \sqrt{N^2 - \sin^2\theta}}$$

$$r = \frac{r_p + r_s}{2} e^{\frac{-16\pi^2 R_q^2 \cos\theta^2}{3\lambda^2}}$$

in which θ is the angle of incidence (82°), r_p is the reflectance for p-polarized light, r_s is the reflectance for s-polarized light and a circularly polarized light has an average of reflectance of both s and p polarized light, R_q^2 is the root-mean-square surface roughness for Debye-Waller correction, and λ is the wavelength of light. We then calculate the Reflection-Absorption (RA) for both polarizations of light from reflectance (r):

$$RA = -\log_{10}(|r|^2)$$

The simulated XUV-MCD spectrum is then given as:

$$MCD = RA_{right} - RA_{left}$$

Table 1: Simulation parameters for MCD calculation

	$Fe^{3+}_{T_d}$	$Fe^{3+}_{O_h}$	$Fe^{4+}_{T_d}$	$Fe^{4+}_{O_h}$
Crystal Field Splitting / eV	-0.6	1.45	-0.6	1.45
Exchange field M / meV	18	-12	18	-12
Slater Integral Reduction	50%	50%	50%	50%
Fano Parameter	5	7	9	9
Minimum Lorentzian Width (minL) / eV	0.1	0.1	0.1	0.1
Lorentzian Broadening (dL) / eV	0.15	0.15	0.15	0.15
Lorentzian Cutoff (cutOff) / eV	48	48	52	52
Energy Offset / eV	-1	1	1	3
CTM4XAS Conversion Parameter / eV	0.006	0.004	0.006	0.004

B. T_d vs O_h Fe^{4+}

To determine whether the light-induced change to the Fe $M_{2,3}$ edge MCD signal appearing around 60 eV represents the contribution of T_d or O_h Fe^{4+}, we simulated contributions from each and compare them to the measured experimental spectrum under illumination. The results are plotted in Figure S7, which shows that the contribution of Fe^{4+} O_h MCD signal provides a good match to the experimental spectrum, but that a contribution from Fe^{4+} T_d MCD signal does not fit the experiment. Even with significant variation of the fitting parameters, it is not possible to simulate the light-induced change to the Fe $M_{2,3}$ edge MCD signal by the inclusion of a Fe^{4+} T_d contribution. From this, we conclude that the hole in the valence band of oxygen couples with the Fe^{4+} O_h sub-lattice. Analysis of the O L_1-edge MCD spectrum below further confirms that the missing electron in O 2p orbital has the same spin as electrons in the filled O_h Fe 3d states, indicating that electronic exchange enables O
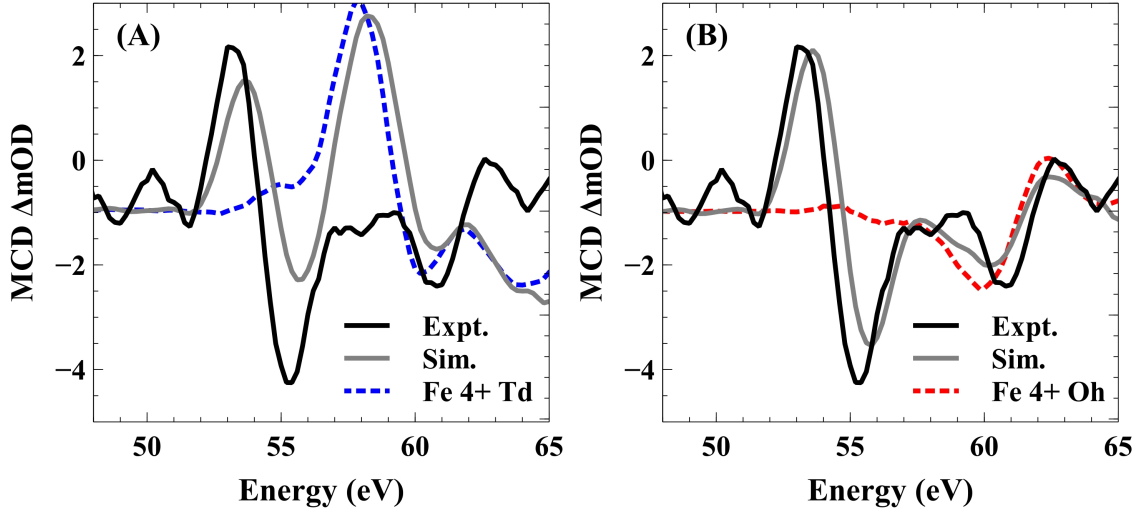
Figure S7: Comparison of experimental and simulated XUV-MCD spectra with illumination including either Fe^{4+} T_d and O_h sublattices

2p hole sharing with O_h but not T_d Fe 3d valence band states.

C. Kramers-Kronig analysis with linearly additive contributions from the two sub-lattices

It is well known that absorption measurements are linearly additive, while reflection measurements are not. However, it is useful to consider the measured XUV-MCD spectrum as the linear addition of O_h and T_d sub-lattices to visualize their individual contributions to the spectrum as depicted in Figure 5 of the main manuscript. To evaluate the validity of this approximation, the following analysis has been performed in which the MCD spectrum is simulated in two ways: First, we take a linear combination of absorption contributions from O_h and T_d sites followed by conversion of a total absorption spectrum to an RA spectrum. Second, we separately calculate RA spectra for O_h and T_d sites, which are then summed to produce a total RA spectrum for YIG. Although the second approach is not rigorously correct, the comparison below shows that these two approaches result in indistinguishable MCD spectra. The reason for the close similarity is that at near-grazing angles, XUV light

experiences total external reflection from a solid surface having negative permittivity at XUV wavelengths such that the primary loss of intensity is a result of absorptive damping of the evanescent field, which scales linearly with sample composition. This analysis indicates that it is appropriate to think of XUV-MCD spectra measured in reflectivity as the result of nearly independent contributions from individual absorbers.
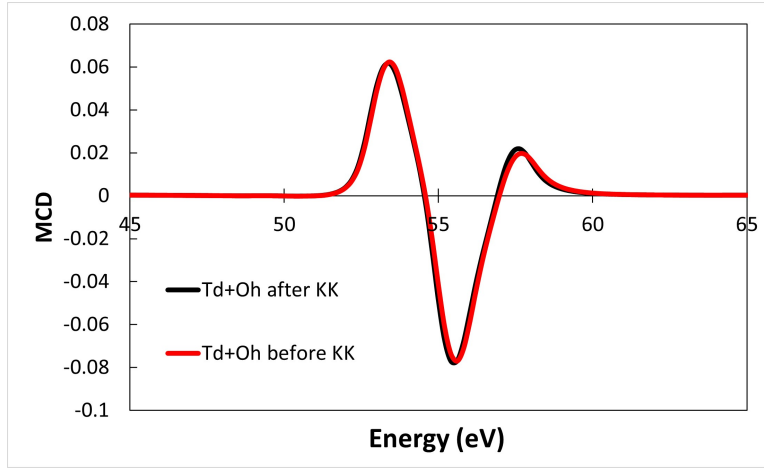
Figure S8: Kramers-Kronig analysis

Figure S8 compares the XUV-MCD spectra of YIG calculated in two ways.

1) The red line combines the simulated k vector values from the T_d lattice and the O_h lattice into one k value vector according to the stoichiometry of YIG.

$$kL = 0.6 * kL_{T_d} + 0.4 * kL_{O_h}$$

$$kR = 0.6 * kR_{T_d} + 0.4 * kR_{O_h}$$

A Kramers-Kronig transformation then converts κ to n, and Fresnel equations are used to obtain the RA spectrum for left and right polarized light.

$$MCD = RA_{right} - RA_{left}$$

2) The black line converts the absorption spectra from the individual sub-lattices into

S12

RA spectra and then combines the RA spectrum from T_d and O_h sub-lattices to create an XUV-MCD spectrum. First, Kramers-Kronig relations are used to convert κ to n, and Fresnel equations are used to obtain the RA spectrum for the T_d sub-lattice only:

$$MCD_{T_d} = RA_{right} - RA_{left}$$

Second, Kramers-Kronig relations are used to convert κ to n, and Fresnel equations are used to obtain the RA spectrum for the O_h sub-lattice only:

$$MCD_{O_h} = RA_{right} - RA_{left}$$

Finally, the two RA spectra are combined to produce a net XUV-MCD spectrum:

$$MCD = 0.6 * MCD_{T_d} + 0.4 * MCD_{O_h}$$

Both methods yield nearly the same spectra as shown in Figure S8.

4. Analysis of O L_1-edge XUV-MCD spectrum

North magnetization is defined such that unpaired electrons in the high spin Fe^{3+} T_d sub-lattice are spin up and electrons in the Fe^{3+} O_h sub-lattice are spin down, consistent with the fact that the T_d sub-lattice controls the net magnetization in YIG. By this definition, the MCD signal is given as the spectrum under north magnetization minus the spectrum under south magnetization while the XUV pulse maintains a constant right circular polarization ($\Delta M_J = +1$). This definition is equivalent to the traditional case where the MCD signal is alternately defined as the difference spectrum for right minus left circularly polarized light under a constant north-facing magnetic field. This first definition is adopted here because it is experimentally easier to switch the sample magnetization compared to switching the XUV polarization during measurements.

In the photoexcited state, the hole resulting from electron excitation to the T_d sub-lattice is long-lived, and this is the species we detect in the O L_1 edge MCD spectrum as described in the main manuscript. This is equivalent to stating that the unpaired electron remaining in the partially filed O 2p valence band is spin aligned with the T_d sub-lattice (i.e., spin up for north magnetization). This electron configuration is depicted for a north-magnetized sample in the lower left panel in Figure S9. The equivalent state for south magnetization is shown in the lower right panel in Figure S9, where the unpaired O 2p electron has a spin down.
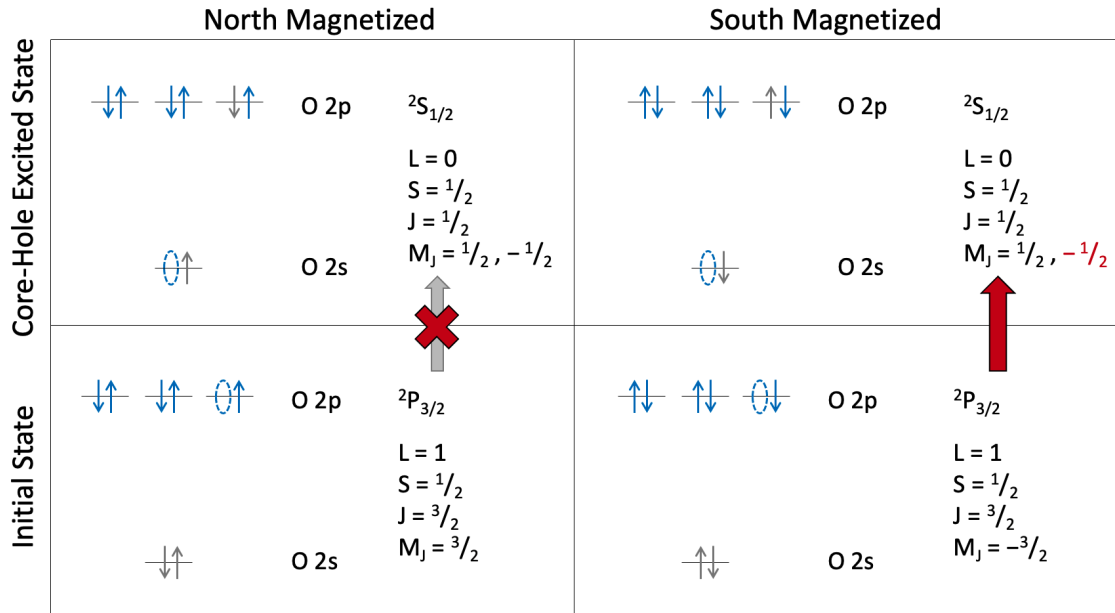
Figure S9: Selection rule for O L_1-edge

Considering now the O L_1 edge or 2s to 2p transition, the top two panels in Figure S9 depicted the corresponding electron configurations for the core-hole excited states associated with a single electron transition under north and south magnetization, respectively. The corresponding term symbols for each ground and core-hole excited state electron configuration are also provided. Taking the selection rules for a single-electron transition as $\Delta J = 0, \pm 1$, and $\Delta M_J = +1$ for right circularly polarized XUV light, it is evident that the L_1 edge transition is forbidden under north magnetization but becomes allowed only under

south magnetization. For this reason, we observe a single dip in the O L_1 MCD spectrum, confirming that the absolute orientation of unpaired electrons in the O 2p valence band are spin aligned with the Fe T_d sub-lattice. This analysis also explains why the associated valence band holes preferentially mix with O_h rather than the T_d Fe 3d valence band states due to the exchange coupling of the hole with the O_h sub-lattice as described in the main manuscript.

References

(1) Janifer, M. A.; Prabagar, C. J.; Sonia, M. M. L.; Pauline, S.; Anand, S.; Ranjini, P. Removal of Heavy Metal (Cadmium) Using Temperature Optimized Novel Rare Earth Garnet (Y3Fe5O12) Through Simple, Robust, and Efficient Adsorption Technique. *Journal of Superconductivity and Novel Magnetism* **2022**, *35*, 2987–2998.

(2) Vind, J.; Malfliet, A.; Bonomi, C.; Paiste, P.; Sajó, I. E.; Blanpain, B.; Tkaczyk, A. H.; Vassiliadou, V.; Panias, D. Modes of occurrences of scandium in Greek bauxite and bauxite residue. *Minerals Engineering* **2018**, *123*, 35–48.

(3) Niederberger, M.; Krumeich, F.; Hegetschweiler, K.; Nesper, R. An iron polyolate complex as a precursor for the controlled synthesis of monodispersed iron oxide colloids. *Chemistry of materials* **2002**, *14*, 78–82.

(4) Sharma, V.; Saha, J.; Patnaik, S.; Kuanr, B. K. Synthesis and characterization of yttrium iron garnet (YIG) nanoparticles-Microwave material. *AIP Advances* **2017**, *7*.

(5) Chen, F.; Zhu, Y.-J.; Wang, K.-W.; Pan, Y.-B. A Simple strategy for preparation of a series of one-dimensional rare earth oxides using rare earth precursors as templates. *Current Nanoscience* **2009**, *5*, 266–272.

(6) Project, T. M. Materials Data on $Y(NO_3)_3$ by Materials Project. **2020**, DOI: `10.17188/1351414`.

(7) Project, T. M. Materials Data on Y_2O_3 by Materials Project. **2020**, DOI: `10.17188/1201184`.

(8) Stavitski, E.; De Groot, F. M. The CTM4XAS program for EELS and XAS spectral shape analysis of transition metal L edges. *Micron* **2010**, *41*, 687–694.

(9) Vasili, H. B.; Casals, B.; Cichelero, R.; Macià, F.; Geshev, J.; Gargiani, P.; Valvidares, M.; Herrero-Martin, J.; Pellegrin, E.; Fontcuberta, J. et al. Direct observation of

multivalent states and 4 f→ 3 d charge transfer in Ce-doped yttrium iron garnet thin films. *Physical Review B* **2017**, *96*, 014433.

(10) Londo, S.; Biswas, S.; Husek, J.; Pinchuk, I. V.; Newburger, M. J.; Boyadzhiev, A.; Trout, A. H.; McComb, D. W.; Kawakami, R.; Baker, L. R. Ultrafast Spin Crossover in a Room-Temperature Ferrimagnet: Element-Specific Spin Dynamics in Photoexcited Cobalt Ferrite. *The Journal of Physical Chemistry C* **2020**, *124*, 11368–11375.

(11) Londo, S.; Biswas, S.; Pinchuk, I. V.; Boyadzhiev, A.; Kawakami, R. K.; Baker, L. R. Ultrafast Optical Spin Switching in Ferrimagnetic Nickel Ferrite (NiFe2O4) Studied by XUV Reflection–Absorption Spectroscopy. *The Journal of Physical Chemistry C* **2022**, *126*, 2669–2678.

(12) Baker, L. R.; Jiang, C.-M.; Kelly, S. T.; Lucas, J. M.; Vura-Weis, J.; Gilles, M. K.; Alivisatos, A. P.; Leone, S. R. Charge carrier dynamics of photoexcited Co3O4 in methanol: extending high harmonic transient absorption spectroscopy to liquid environments. *Nano Letters* **2014**, *14*, 5883–5890.

(13) Vura-Weis, J.; Jiang, C.-M.; Liu, C.; Gao, H.; Lucas, J. M.; De Groot, F. M.; Yang, P.; Alivisatos, A. P.; Leone, S. R. Femtosecond M2, 3-edge spectroscopy of transition-metal oxides: photoinduced oxidation state change in α-Fe2O3. *The Journal of Physical Chemistry Letters* **2013**, *4*, 3667–3671.

(14) Shin, S.; Suga, S.; Kanzaki, H.; Shibuya, S.; Yanaguchi, T. Multiplet structures of the inner core absorption spectra of KMnF3 and KCoF3 measured by synchrotron radiation. *Solid State Communications* **1981**, *38*, 1281–1284.

(15) Cirri, A.; Husek, J.; Biswas, S.; Baker, L. R. Achieving surface sensitivity in ultrafast XUV spectroscopy: M2, 3-edge reflection–absorption of transition metal oxides. *The Journal of Physical Chemistry C* **2017**, *121*, 15861–15869.